JACS
JOURNAL OF THE AMERICAN CHEMICAL SOCIETY
pubs.acs.org/JACS
Article

Stabilizing All-Solid-State Li–S Batteries by a Polysulfide-Repelling and Anode-Protecting Self-Segregated Trilayer Polymer Electrolyte

Hao Lyu, Xin Gao, Lukas Michalek, Tianyang Chen, Weilai Yu, Carina Yi Jing Lim, Jacob Florian, Luca Mondonico, Wenbo Zhang, Susmita Sarkar, Pu Zhang, Yuran Shi, Kuan-Yu Lin, Sheng-Lun Liao, Xueli Zheng, Jian Qin, Yi Cui,* and Zhenan Bao*

Cite This: J. Am. Chem. Soc. 2026, 148, 5275–5286
Read Online
ACCESS | Metrics & More | Article Recommendations | Supporting Information

ABSTRACT: Rational management of lithium polysulfide (LiPS) transport is essential for stable, high-energy-density Li–S batteries. We introduce a freestanding, self-segregated trilayer polymer electrolyte (TLE) that forms two layers of nanometer-thin, ion-selective coatings at the cathode and anode interfaces by autonomous phase separation of two immiscible polymers while preserving a highly conductive bulk matrix. In Li–S cells, these coatings simultaneously repel dissolved LiPS at the sulfur cathode and stabilize lithium plating and stripping at the Li metal anode without sacrificing ion transport. Operando optical cell monitoring and theoretical modeling reveal that the dual-functional coatings are responsible for stable Li metal anode operation and effective shuttle suppression. The TLE enables an initial discharge capacity of 1369 mAh g^{-1} (81.7% of theoretical) and maintains a stable capacity over 50 cycles at 0.2C. Fabricated by a single-step casting process, this scalable electrolyte membrane offers a practical route to durable, all-solid-state Li–S batteries.

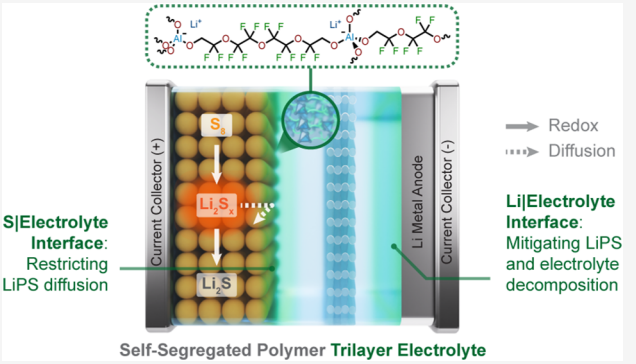

INTRODUCTION

Rechargeable lithium–sulfur (Li–S) batteries are among the promising solutions to approach high-energy-density electrochemical energy storage due to their exceptionally high theoretical energy density (~2600 Wh kg^{-1}) and the natural abundance of sulfur cathodes.[1−8] However, the dissolution and migration of intermediate lithium polysulfides (Li_2S_x, $2 \leq x \leq 8$) during cycling, commonly termed as polysulfide shuttling, lead to active material loss, low Coulombic efficiency, and rapid capacity fading.[5,9−12] This shuttle effect not only degrades the sulfur cathode but also corrodes the lithium metal anode, undermining the long-term stability of Li–S cells.

To address the polysulfide shuttle issue, a range of strategies have been developed, including engineered carbon hosts, functional interlayers, electrolyte additives, and separator coatings.[13−19] One of the most promising routes is the transition to solid-state Li–S batteries, where solid electrolytes, whether inorganics, polymers, or hybrid composites, can inherently block dissolved sulfur species and enhance safety.[20,21] Among solid-state architectures, inorganic and polymer-inorganic composite-based electrolytes offer effective prevention of LiPS shuttling and high ionic conductivities, but interfacial complexities and processability remain to be resolved. Polymer-based electrolytes offer unique advantages, including facile processing, operation at low to moderate pressures, and the potential for flexible, lightweight cell designs.

Nevertheless, polymer electrolytes face two critical challenges in Li–S battery systems: (i) Despite the reduced polysulfide solubility in the solid matrix, complete suppression of polysulfide shuttling remains elusive. (ii) Stabilizing the lithium–metal anode against interfacial polymer degradation and subsequent dendrite growth is still problematic. Realizing both effective polysulfide confinement and robust Li-metal protection within a single-component polymer electrolyte has proven difficult, in that modifications improving one function often compromise the other, such as ion selectivity and conductivity.[22,23]

Here, we introduce a trilayer polymer electrolyte design that leverages spontaneous phase segregation of two immiscible polymers to form discrete, nanometer-thin functional coatings at both the cathode and anode interfaces while preserving a high-conductivity polymer matrix in the bulk. This architecture simultaneously inhibits polysulfide migration and stabilizes

Received: October 13, 2025
Revised: December 7, 2025
Accepted: January 26, 2026
Published: February 2, 2026

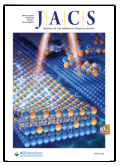

https://doi.org/10.1021/jacs.5c18042
J. Am. Chem. Soc. 2026, 148, 5275−5286

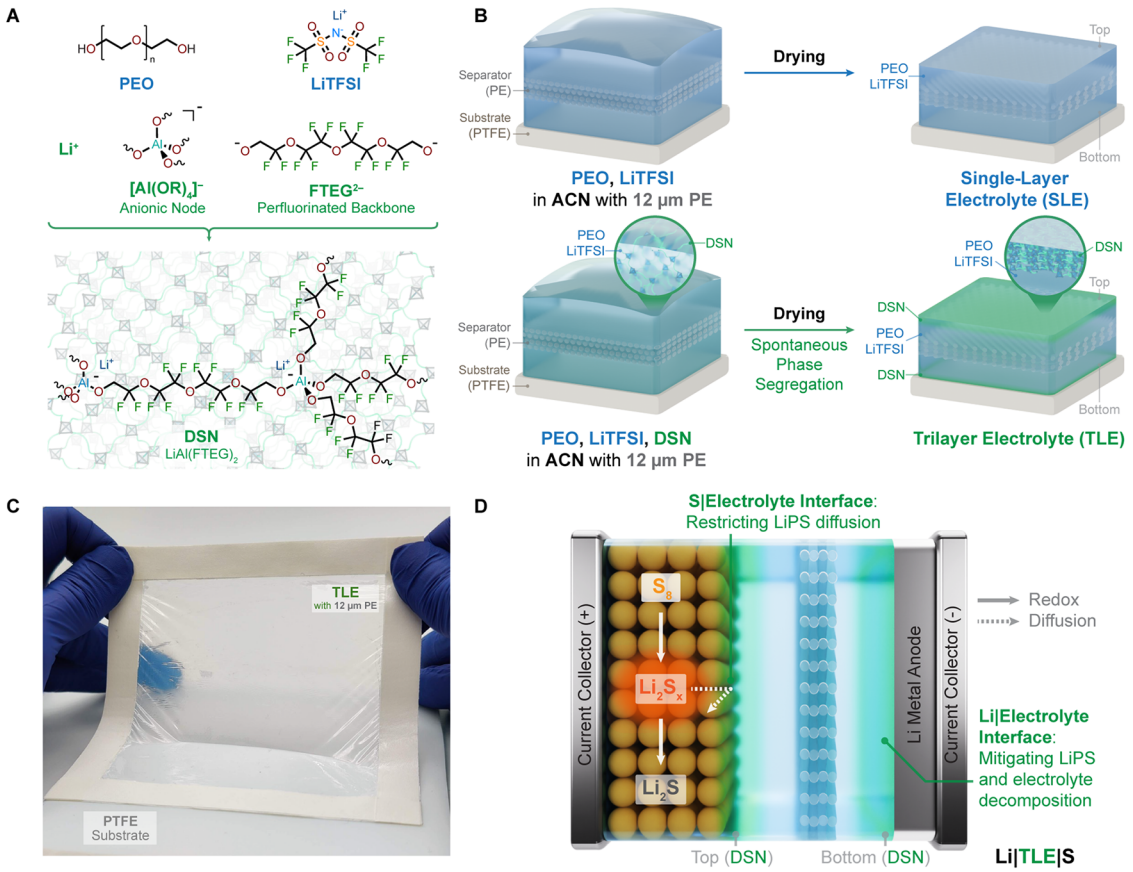

Figure 1. Design and preparation of freestanding self-segregated polymer solid-state electrolyte for Li−S batteries. (A) Chemical structures of electrolyte components and schematic representation of the composition of DSN. (B) The preparation of SLE and TLE (7 wt % DSN) electrolytes through a single-step dropcasting method. (C) Photo of a TLE electrolyte film of 90 mm × 90 mm size (81 cm^2) cast in a soft tape frame. (D) Schematics of S-containing species in Li−S batteries with TLE electrolyte during discharge, and how self-segregated DSN layers mitigate the shuttling issues by interacting with polysulfide species and stabilizing the Li metal anode. The top and bottom surfaces of SLE and TLE, when assembled into the Li−S cells, are marked corresponding to the surfaces marked in (B). The structure of DSN in panels (B) and (D) is marked by blue tetrahedra, representing $[Al(OR)_4]^-$ nodes, and green splines, representing FTEG backbones to illustrate its network structure. For conciseness, the self-segregated DSN layers are represented as green gradient layers in the following parts of the discussion. ACN, acetonitrile.

lithium plating and stripping without sacrificing overall ion transport, offering a new platform for high-performance, all-solid-state Li−S batteries. We further designed a new construction of optical cells for *operando* monitoring of S-containing species in the Li−S cell. In addition, compared to conventional multistep fabrication, our freestanding self-segregated trilayer polymer electrolyte can be prepared within a simple, single-step casting process, facilitating potential scalability in the future.

RESULTS AND DISCUSSION

Polysulfide Repulsion by an Ion-Selective Polymer Network Coating

We use a state-of-the-art solid-state polymer electrolyte composed of poly(ethylene oxide) (PEO), lithium bis-(trifluoromethanesulfonyl)imide (LiTFSI), and a 12 μm porous polyethylene (PE) separator as mechanical support, as the reference single-layer polymer electrolyte (SLE, Figure 1A,B).[16,24−27] Previous studies observed limited cyclability in such systems due to unrestricted polysulfide shuttling effect and Li metal anode destabilization.[16] To address this issue, we introduce a dynamic, ion-selective polymer network (DSN, Figure 1A) to form the spontaneously phase-separated trilayer electrolyte (TLE). The DSN network features anionic $[Al(OR)_4]^-$ (R, fluorinated alkoxide backbones) nodes, flexible fluorinated backbones (1*H*,1*H*,11*H*,11*H*-perfluorotetraethylene glycoxide, $FTEG^{2-}$), and Li^+ counterions, and was synthesized according to our reported procedures.[28]

DSN is immiscible with PEO-LiTFSI but cosoluble in acetonitrile (ACN), allowing a homogeneous solution of both to be used for a facile and scalable dropcasting preparation (Figure 1B). Upon casting to the PE separator, spontaneous phase segregation between PEO, LiTFSI, and DSN takes place during solvent evaporation to form the trilayer structure. The immiscible nature of DSN and PEO was envisioned to drive the formation of thin, continuous, and protective DSN coating layers at the top and bottom surfaces of the TLE, which later serve as the interface between TLE and both electrodes (Figure 1B,C, see also Supporting Information, SI, Section S1 and Figures S3 and S4). We previously confirmed that DSN can protect the Li metal anode when paired with liquid electrolytes by maintaining a conformable coating layer, blocking solvent transport and decomposition at Li metal.[28] In this context, we examine its protective effect on both the S cathode and Li metal anode when paired with the PEO-LiTFSI matrix in an all-solid-state configuration.

We envision that DSN regulates LiPS diffusion by limiting LiPS solubility through (1) electrostatic repulsion by the

https://doi.org/10.1021/jacs.5c18042
J. Am. Chem. Soc. 2026, 148, 5275−5286

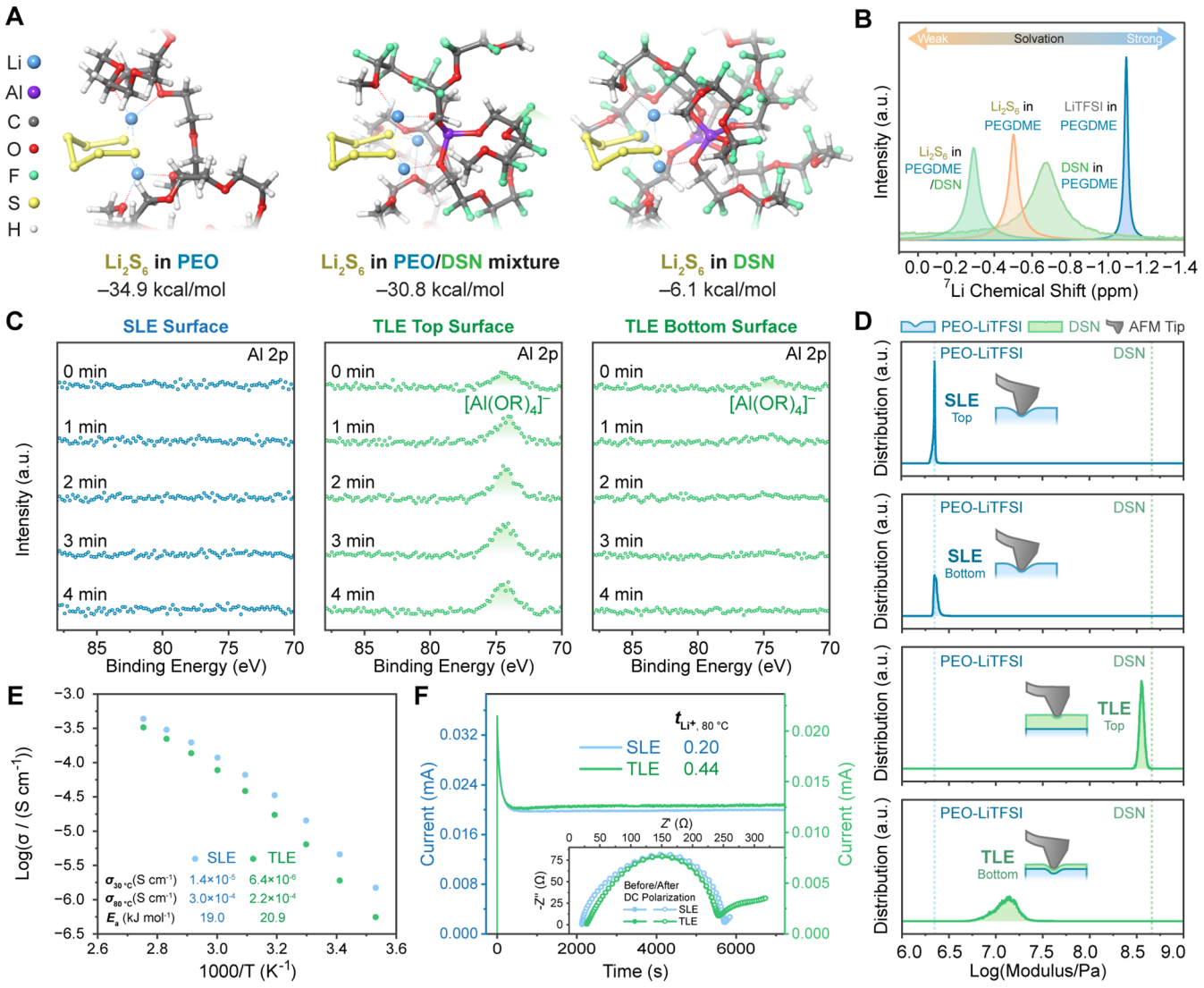

Figure 2. Structural study of SLE, TLE, and their interaction with lithium polysulfide species. (A) DFT calculated atomic structures of Li_2S_6, a representative LiPS, interacting with molecular fragments representing PEO and DSN. Ionic coordination interactions are marked in dashed lines. (B) ^{7}Li NMR spectra of Li_2S_6 in liquid analogue mixtures, showing the weakening of LiPS solvation by DSN. (C) High-resolution Al 2p XPS sputtering depth profiles of SLE and top and bottom surfaces of TLE films. (D) Log(Modulus) histogram of AFM PeakForce QNM measurements of top and bottom surfaces of SLE and TLE. The schematics represent possible film structures near the surface corresponding to the mechanical response to the AFM tip, a combined result of intrinsic modulus differences and the substrate effect. Blue and green dashed lines are provided as modulus references for PEO-LiTFSI and DSN, respectively. (E) Ionic conductivity of SLE and TLE at temperatures ranging between 10 and 90 °C. (F) Chronoamperometry traces and EIS spectra (inset) of LTN measurements of SLE and TLE electrolytes.

anionic $[Al(OR)_4]^-$ nodes and (2) reduced binding affinity by the perfluorinated backbones of the network. To confirm this, we first studied LiPS solvation by DSN through density functional theory (DFT) calculations at the BPW91/6−31G+* level[29,30] among species in SLE, TLE, and LiPS, using their representative molecular fragments (Scheme S1). Qualitative comparison of the thermodynamic favorability of solvation was performed by calculating the potential energy changes as a result of LiPS interacting with the electrolyte components (SI Section S2). LiPS interacts with PEO through favorable chelation between Li^+ and adjacent ether oxygen atoms of the PEO chain. In the presence of DSN, each Li^+ in LiPS interacts with one oxygen atom of the $[Al(OR)_4]^-$ nodes instead, disrupting chelation to PEO due to its geometric constraints (Figure 2A). In addition, the binding of LiPS competes with the original counterion Li^+, further inducing energy penalties for the interaction. As a result, the potential energy calculation yields a −34.9 kcal/mol interaction energy of LiPS in a PEO-rich environment (Figures 2A and S6), a reduced −30.8 kcal/mol interaction energy in a PEO/DSN mixture or at their interface (Figures 2A and S7), and a drastically weakened interaction energy of −6.1 kcal/mol in a DSN-rich environment (Figures 2A and S8).

To experimentally corroborate this prediction, liquid-state ^{7}Li NMR spectroscopy was conducted to probe the interaction between PEO, LiTFSI, DSN, and LiPS (Figure 2b and Supporting Text Section S3). Anhydrous dimethyl-terminated polyethylene glycol (PEGDME) was used as a solvent closely analogous to PEO, representing its role of solvation in SLE or TLE. Li^+ in LiTFSI in PEGDME displays an upfield chemical shift of −1.09 ppm, corresponding to its strong Li^+ solvation. Li^+ in DSN showed a signal at a lower-field value of −0.67 ppm

https://doi.org/10.1021/jacs.5c18042
J. Am. Chem. Soc. 2026, 148, 5275−5286

due to weakened solvation. A representative compound of LiPS species, Li_2S_6, displays a chemical shift of −0.50 ppm in PEGDME. When dissolved in PEGDME with 7 wt % DSN, the Li^+ signal shifted further downfield to −0.29 ppm, indicating a weakening solvation of Li_2S_6 by the presence of DSN. The broadness of the Li_2S_6 peak also shows a slight increase compared to Li_2S_6 in PEGDME, further indicating the unfavorable binding of Li_2S_6 to the DSN network. Both phenomena agree with the calculation result of unfavored interactions between the DSN and LiPS species in the electrolyte solution.

Autonomous Interfacial Layer Formation by Spontaneous Phase Separation

Phase Separation Drives Nanometer-Thin Interfacial Layer Formation. With the structural origin of unfavorable LiPS interaction (i.e., LiPS repulsion) by DSN established, we move on to confirm the accumulation of DSN at the electrolyte surfaces. We first use differential scanning calorimetry (DSC) to characterize SLE and TLE, which indicated minimal mixing between DSN and PEO in TLE (Supporting Text Section S4 and Figure S9). Specifically, both SLE and TLE exhibited almost identical glass-transition temperature (T_g: SLE, −43.4 °C; TLE, −43.4 °C) and melting point (T_m: SLE, 41.7 °C; TLE, 43.0 °C) values, indicating that both the amorphous and crystalline regions of PEO in the TLE experience minimal influence from DSN. This behavior suggests a low miscibility between PEO-LiTFSI and DSN, a driving force for the formation of the proposed vertically phase-separated trilayer structure in the TLE. To confirm this, depth profiling of the surfaces of SLE and TLE electrolyte films was performed using X-ray photoemission spectroscopy (XPS) at Al 2p binding energy with gas cluster ion beam (GCIB) sputtering.[31,32] As an element unique to DSN, Al was used to probe the presence of DSN in the electrolyte films. In the absence of DSN, Al 2p signals were not found on the SLE top or bottom surfaces, as expected. These signals were found only on both the top and bottom surfaces of TLE, which can be attributed to $[Al(OR)_4]^-$ nodes in DSN (Figure 2C and SI Section S5). The Al signal at the TLE top surface remained undiminished throughout the 4 min sputtering, indicating a DSN-containing layer thicker than the sputtering depth. In contrast, the Al signal at the bottom surface of TLE diminished after 3 min of sputtering, indicating a thinner DSN layer compared to the profiled depth. In both cases, the Al element was found at the same binding energy, indicating a likely uniform chemical environment throughout the profiled depth. This observation corresponds to a chemically intact presence of DSN, functioning as an interfacial coating at both the top and bottom surfaces of the TLE.

Mechanical studies on the electrolytes were performed using atomic force microscopy (AFM) in PeakForce Quantitative Nanomechanics (QNM) mode, which provides a noninvasive approach to determine and validate the chemical identity and relative thickness of the surface coatings. Height and Derjaguin−Muller−Toropov (DMT) modulus[33] mapping were performed on the top and bottom surfaces of SLE and TLE specimens (Figures 2D and S18A and SI Section S6), which all showed homogeneous profiles across the scanned areas. However, a distinctively higher modulus can be found on the top and bottom surfaces of TLE compared to those of SLE. Compared to DSN spin-coated on a rigid glass substrate as a reference (5.0×10^8 Pa, Figure 2D), both the top and bottom surfaces of SLE showed a consistently low modulus at 3.2×10^6 Pa with narrow distributions. In contrast, the TLE top surface showed a modulus distribution peaking at 3.6×10^8 Pa, which is within the range of sample variation to the pure DSN reference. This result indicates the presence of a substantial layer almost fully composed of DSN. Comparatively, the TLE bottom surface exhibits a wider distribution of modulus, peaking at 1.6×10^7 Pa. This observation can be attributed to the relatively less uniform bottom surface of TLE due to the substrate unevenness, as well as the dependence of the DMT modulus on the thickness of the layers in the film. As is illustrated in Figure 2D, the modulus of a relatively rigid but thin (DSN) surface film can be underestimated on a relatively soft (PEO-LiTFSI) substrate by dissipating more deformation. We thus attribute this modulus to a much thinner DSN layer on the bottom surface of the TLE.

We next determined the thickness of the DSN coatings at the top and bottom surfaces of TLE using mechanically stretched samples, where cracks formed at the surface DSN layers by applying a small strain (<2−5%, by peeling the film off from the PTFE substrate, Figures S18B and 1C). One-dimensional line profiles of height and log(DMT modulus) of the TLE top surface reveal a ∼50 nm thick layer of 1.1×10^8 Pa modulus, attributable to DSN, and a valley region with 2.7×10^6 Pa modulus, attributable to the bulk PEO-LiTFSI electrolyte (Figure S18D). At the TLE bottom surface, a less distinctive height difference of ∼15 nm can be found at the crack, yet a distinguishable modulus difference was observed (2.3×10^7 Pa, corresponding to a thin DSN layer, and 7.2×10^6 Pa, corresponding to bulk PEO-LiTFSI, Figure S18F). Combined with the above-mentioned DSC and XPS results supporting distinctive phase separation, we establish that the TLE electrolyte is composed of a bulk PEO-LiTFSI electrolyte matrix covered with ∼50 nm DSN coating at the top surface and ∼15 nm at the bottom surface, a result of the spontaneous phase segregation.

When sandwiched between polymer-infiltrated S cathodes (SI Section S1) and Li metal anodes in an optimized configuration, TLE contacts the S cathode by the top surface and Li metal anode by the bottom, both through a DSN-rich polymer layer (noted in Figure 1B,D). We thus anticipate that on the S cathode side, the polysulfide diffusion into the PEO-LiTFSI bulk will be suppressed by the thicker DSN layer from the TLE top surface, while on the Li metal anode side, the thin DSN layer from the TLE bottom will face Li metal instead of PEO-LiTFSI, reducing electrolyte degradation and solid-electrolyte interphase (SEI) accumulation to maintain stable cycling (Figure 1D).

Retention of Li^+ Ion Conductivity while Increasing Li^+ Transference Number. With the trilayer structure established, we first examined the ion transport of TLE compared to the reference SLE. As mentioned before, a major challenge of using single-ion conducting polymers as all-solid-state electrolytes is the slow ion transport due to the strong association of Li^+ with the anionic polymer backbones.[34−37] By enriching with an ion-selective DSN coating[28] only at nanometer-thin layers at the electrolyte surfaces in TLE, we envision that the bulk ion conduction properties of PEO can be mostly retained. This is confirmed by testing the ionic conductivity of both SLE and TLE electrolytes between 10 and 90 °C using electrochemical impedance spectroscopy (EIS, Figure 2E and SI Section S7 and Figures S19 and S20). The ionic conductivity of SLE at around room temperature (30 °C) was 1.4×10^{-5} S/

https://doi.org/10.1021/jacs.5c18042
J. Am. Chem. Soc. 2026, 148, 5275−5286

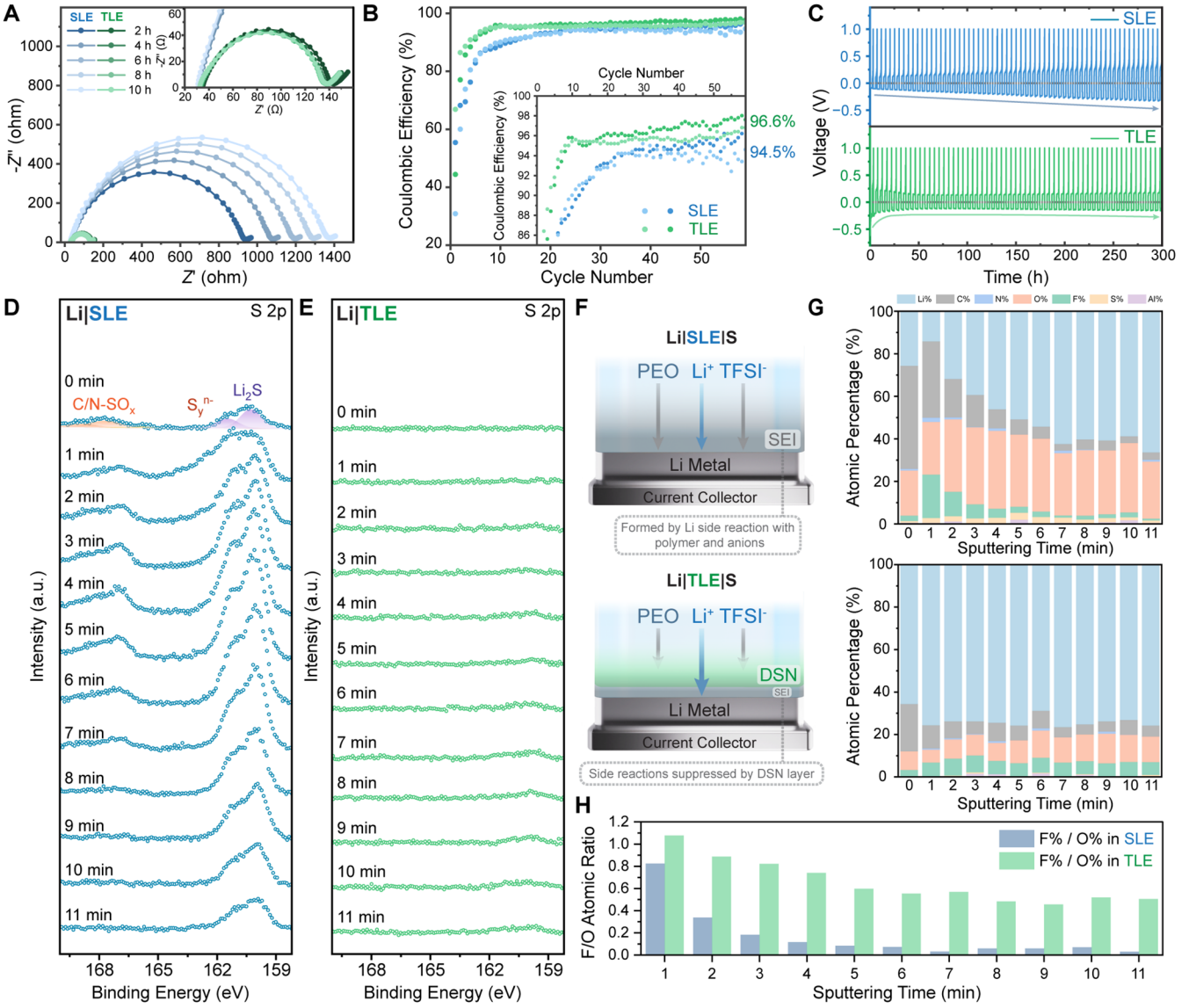

Figure 3. Comparison of ion conduction and Li metal anode stability between SLE and TLE. (A) EIS impedance evolution in open circuit resting of Li|SLE|Li and Li|TLE|Li symmetric cells at 80 °C. (B) Cycling Coulombic efficiency in Li||Cu cells operating at 80 °C (0.2 mA/cm^2, 0.5 mAh/cm^2, 1 cm^2), where two parallel cell results are provided in different shades for clarity. (C) Cycling voltage profiles of Li||Cu cells, whose trend of evolution is highlighted by arrows, respectively. (D, E) Depth profiles of high-resolution S 2p XPS spectra and (G) atomic elemental composition of Li metal anode surfaces disassembled from Li|SLE|S or Li|TLE|S cells after resting for 24 h and discharging at 0.05C at 80 °C. Li|TLE shows much higher Li content, signifying the lower amount of SEI generated during this process due to the stabilization of the DSN layer, which is conceptually illustrated in panel (F). Panel (H) further provides the atomic ratio between F and O elements in the XPS depth profiles.

cm, while TLE displayed a slight reduction to 6.4×10^{-6} S/cm. At elevated temperature (80 °C), SLE displayed an ionic conductivity at 3.0×10^{-4} S/cm, and TLE showed a more comparable and still slightly lower ionic conductivity at 2.2×10^{-4} S/cm. We thus selected 80 °C as the operating temperature for the Li−S battery to ensure sufficient ion conductivity and for all following electrochemical studies to align the conditions. Arrhenius analysis applied to the temperature-dependent ionic conductivity curves yielded an activation energy for Li^+ conduction of 19.0 kJ/mol in SLE, and 20.9 kJ/mol in TLE (Figures S21 and S22 and Table S1). These results indicate that the thin DSN coatings in TLE have a minor influence on its ionic conductivity and its kinetic barrier of Li^+ ion transport, corroborating the phase separation that maintains the ion conduction properties of the bulk electrolyte. By contrast, a substantial difference was found in the lithium transference number (t_{Li^+}, LTN) of both electrolytes at 80 °C, evaluated by a customized Bruce-Vincent method (SI Section S8.1).[38] The t_{Li^+} value was 0.44 in TLE, more than double the value of 0.20 for the SLE reference (Figure 2F). This result can be attributed to the thin ion-selective conductive DSN coatings (t_{Li^+} = 0.8) that helped improve the selective transport of Li^+ ions against anionic species, a characteristic function of the anionic $[Al(OR)_4]^-$ nodes that are localized only at the electrolyte interface.

Protection of Li-Metal Anode

Static Protection of Li Metal Anode against Chemical Corrosion. With the electrolyte structure of TLE and its ion conduction properties established, we evaluate its protection role at the Li anode and the S cathode of the Li−S battery. In our previous study, DSN protects Li metal anodes in

https://doi.org/10.1021/jacs.5c18042
J. Am. Chem. Soc. 2026, 148, 5275−5286

carbonate-based liquid electrolyte by blocking solvent molecules due to the solvent-phobic perfluorinated backbone structure, and its single-ion conductivity reducing the decomposition of anions.[28] Here, we examine DSN's protection of Li metal anode in two major aspects, including (i) blocking side reactions between polymer electrolyte and Li metal anode during static resting and (ii) suppressing shuttled LiPS species from reaching Li during Li−S cell cycling. The first aspect of protection was evaluated in Li||Li symmetric cells, where SLE and TLE electrolytes were monitored in open-circuit resting at 80 °C, while EIS measurements were repeated every 2 h in a 10 h resting duration (Figure 3A and SI Section S8.2). Both Li||Li cells with SLE and TLE electrolytes displayed a similar and stable bulk impedance of 31.3 ± 0.6 Ω/cm^2 for SLE and 33.4 ± 1.0 Ω/cm^2 for TLE, attributed to their similar bulk ionic conductivity. However, the Li|SLE|Li cell exhibited a significantly higher interfacial impedance of 940 Ω at the second hour, which further evolved to 1379 Ω (46.8% increase than the second hour) at the 10th hour. This result indicates that SLE continuously reacted with Li during the resting period, resulting in the continually increasing interfacial impedance observed. By contrast, the Li|TLE|Li cell exhibited a 144 Ω interfacial impedance at the second hour. It did not further increase by the 10th hour (Figure 3A inset). This pronounced contrast indicates that the unstable interface between SLE and Li metal due to the intrinsic reactivity of SLE (i.e., PEO and TFSI$^-$) can be effectively stabilized by the DSN in TLE. We further corroborate this protection effect with XPS compositional studies with argon ion sputtering of Li metal anodes disassembled from open-circuit resting Li||S cells (72 h at 25 °C, SI Section S5 and Figures S10−S13). After resting, the Li|SLE surface was populated by partial degradation products of LiTFSI (Figure S10), forming C−SO$_x$ or N-SO$_x$ species and further reduction products, such as Li_2S_2, organic SEI components signified by C−O, C═O, C−C/H (Figure S11), LiOH (Figure S12), and LiF (Figure S13) throughout the probed depth profile. By contrast, the Li|TLE interface showed much fewer signals of partial decomposition products of LiTFSI (Figure S10), organic components (Figure S11), LiOH (Figure S12), and LiF (Figure S13). A quicker signal decay was also observed throughout the sputtering series, signifying a thinner SEI layer resulting from fewer decomposition reactions due to the protection by the DSN coating. This result is in good agreement with the contrast of interfacial impedance evolution between Li|SLE|Li and Li|TLE|Li cells observed by the EIS measurements (Figure 3A).

Dynamic Protection of Li Metal Anode during Cell Cycling. Quantitative evaluations of cycling efficiency and stability of SLE and TLE in Li||Cu half cells were first performed at 80 °C at a 0.2 mA/cm^2 current density and 0.5 mAh/cm^2 areal capacity (Figure 3B). Cycling Coulombic efficiency (CE) displays a faster activation and higher average in TLE compared to SLE, suggesting a longer-lasting protection by the DSN surface coating present in TLE. Specifically, Li|SLE|Cu cells reached an average CE of 89.4% after 10 cycles and required a further ∼20 cycles to reach a plateau. In contrast, the Li|TLE|Cu cell CE reached 95.5% and stabilized in the first 10 cycles. The averaged CE of the 46th−55th cycles was calculated as 94.5% for SLE and 96.6% for TLE. In addition, the voltage profile of Li|SLE|Cu cells showed a gradual overpotential increase, a result attributable to side reactions between PEO, TFSI$^-$ and the electrode, and subsequent accumulation of extra SEI, while TLE cells showed a stable voltage profile for >300 h without a significant increase (Figure 3C). Detailed voltage profiles of the 10th and 55th cycles are compared between SLE and TLE to characterize the different extent of overpotential evolution (Figure S23 and SI Section S8.3). The SLE system exhibited a 0.09 V overpotential in the 10th cycle, while it was ∼0.11 V in TLE. However, in the 55th cycle, the overpotential in the SLE system increased to >0.2 V, while TLE only increased from ∼0.11 V to ∼0.12 V.

The above results established the effective protection of Li metal anodes with TLE. We further characterized the compositional changes at the Li-electrolyte interfaces with the presence of DSN in Li||S cells to find its structural origin. XPS depth profiling with argon ion sputtering was performed on Li metal anodes disassembled from Li|SLE|S or Li|TLE|S cells after initial discharge (resting 24 h at 80 °C, discharging at 0.05C until 1.5 V at 80 °C). For all C-rate notations, 1C = 1675 mA/g S (Figure 3D−G and S14−S17). A more extensive depth profiling series was applied to the Li metal anodes after resting and discharging at a 0.05C rate at 80 °C to reveal the SEI composition under the influence of LiPS shuttling. High-resolution S 2p spectra of Li|SLE displayed features of polysulfide species (S_y^{n-}) alongside partial decomposition of LiTFSI (Figure 3D), which are absent in Li|TLE throughout the sputtering series (Figure 3E). Atomic composition also suggests that a large population of SEI components (C, N, O, F, S, ∼75%) are present on the Li|SLE surface because of reactions between PEO, TFSI$^-$, and LiPS with Li metal. By contrast, <35% non-Li elements were found on the Li|TLE surface, which were further reduced along the sputtering depth (Figures 3G and S15−S17). Particularly, the Li 1s spectra of Li|TLE surfaces were also found to be dominated by metallic Li, with *a* significant plasmon loss feature identifiable from 0 to 11 min of sputtering, which was not identifiable in the Li|SLE sputtering series (Figure S14). Furthermore, the atomic ratio between F element (degradation from TFSI$^-$ anion) and O element (degradation from both PEO polymer and TFSI$^-$ anions) and its changes throughout the sputtering profile suggest the different origins of the SEI as well. The F%/O% ratio in Li|SLE quickly decayed to <0.2 while their sum (F% + O%) remained between 30% and 50% of all atoms, indicating that components from PEO decomposition reactions dominated the SEI components on Li|SLE. In Li|TLE, the F%/O% ratio remained >0.4 and significantly larger than Li|SLE, and their sum (F% + O%) was less than 25% throughout the sputtering series (Figure 3H).

Combining the XPS findings with the analyses above on S 2p spectra, we conclude that both polymer- and anion-derived SEI generation were suppressed by the presence of the nanometer-thick DSN coating layer in TLE, which enables a stable interface between Li metal anode and polymer electrolyte over time at ambient and elevated operating temperatures (Figure 3F). We attribute this to DSN's selective transport of Li$^+$ ion and fewer solvent molecules, which thus suppresses solvent decomposition at the Li-electrolyte interface. The phase separation of DSN ensures its conformable coverage of the Li metal anode, allowing these protective effects to be localized at the Li-electrolyte interface. Hence, we confirm the effectiveness of our self-coating design strategy on the anode side. We proved that the stabilization effect of DSN as a polymer coating designed for liquid electrolytes can be translated to enhancing Li metal anode stability with solid

https://doi.org/10.1021/jacs.5c18042
J. Am. Chem. Soc. 2026, 148, 5275−5286

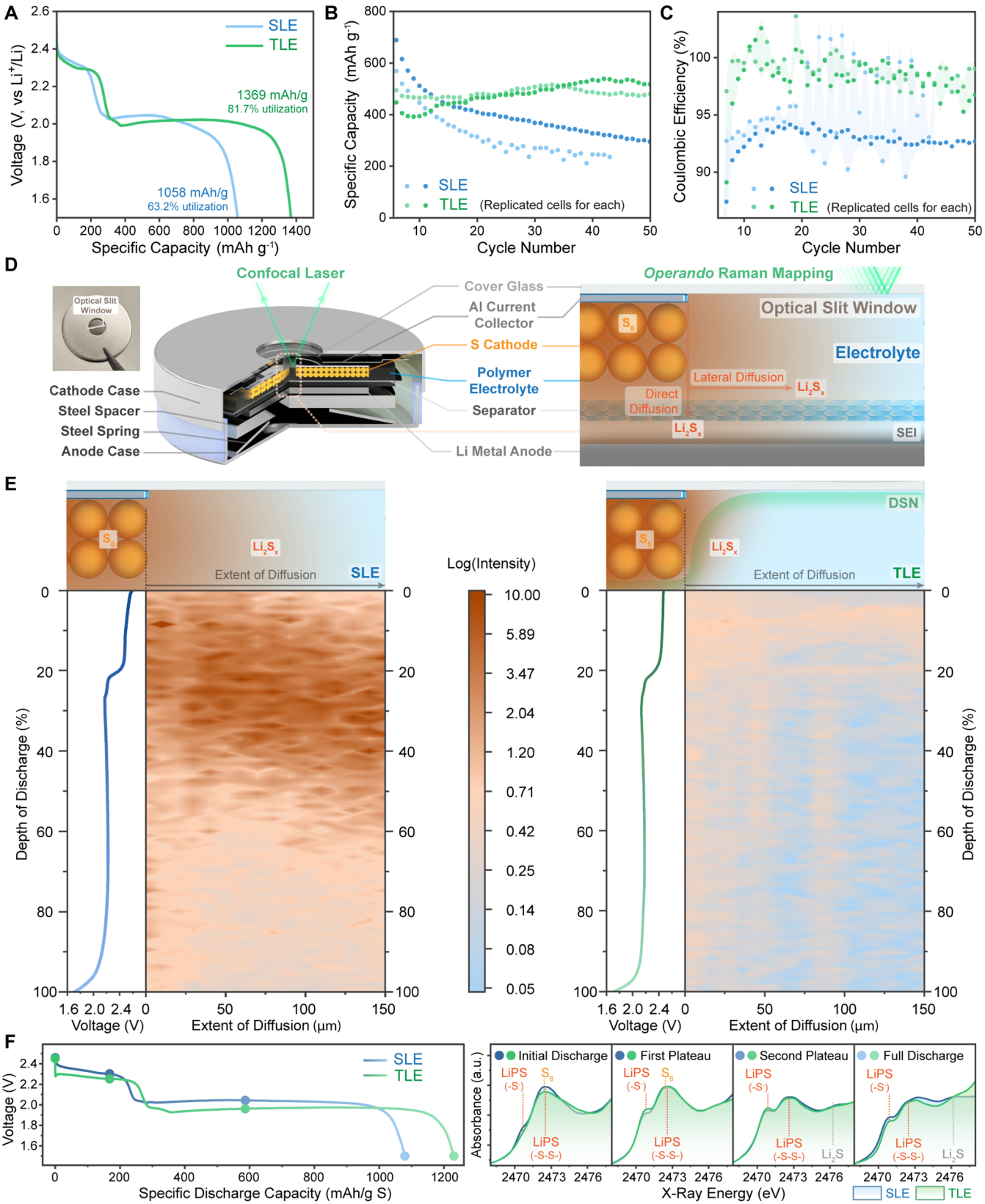

Figure 4. Comparison of S cathode performance and observation of the suppression of LiPS diffusion. (A) Capacity-voltage curve of first (0.05C) discharge step, (B) specific discharge capacity, and (C) Coulombic efficiency of battery cycling in Li|SLE|S or Li|TLE|S cells (1 mg S/cm^2, 50% S, E/S ≈ 9 by electrode area, see SI Section S1; 80 °C, 1.5−2.8 V, charge and discharge at 0.2C). Different shades of symbols in panels (B, C) denote replicated cell results. Error bands in panel (C) denote the standard deviation of replicated cells. (D) Digital image and cross-sectional structure of an optical Li−S coin cell assembly. A zoomed-in view of the cell structure at the optical slit window, the direct and lateral diffusion of LiPS within the electrolyte (brown), and *operando* Raman mapping light paths are provided on the right. (E) *Operando* polysulfide Raman signal (~389 cm^{-1}) map of the exposed SLE (left) and TLE (right) electrolyte in the optical slit, showing the extent of diffusion along the depth of discharge,

https://doi.org/10.1021/jacs.5c18042
J. Am. Chem. Soc. 2026, 148, 5275−5286

Figure 4. continued

comparing SLE and TLE. Voltage profiles along DoD are provided alongside the Raman maps. (F) *Ex situ* S K-edge XANES spectra of S cathodes and voltage profiles of the first discharge step at 0.05C of standard Li|SLE|S (blue) and Li|TLE|S (green) cells. XANES data for TLE are provided in SLE subpanels (bottom left) with low opacities for ease of comparison, and vice versa (bottom right). Highlighted points on the voltage traces correspond to the DoD for each subpanel, with XANES traces in the same color.

polymer electrolytes as well, laying a solid ground for further tests of Li−S full cell systems.

Improvement of S Cathode

Evaluating the Improvements of Sulfur Utilization and Cycling Stability. Li||S full cell cycling experiments were performed at 80 °C. The voltage profile of the first cycle (0.05C) was compared between bare SLE and TLE electrolytes (Figure 4A). For the first discharge voltage plateau (corresponding to S_8 to Li_2S_4 conversion),[39] the voltage of TLE at ∼2.3 V was slightly lower compared to SLE, attributable to the slightly lower ion conductivity. However, TLE displays a 23% increase in capacity, corresponding to improved capacity utilization of the transformation between elemental S and long-chain polysulfides. Furthermore, the second plateau at ∼2.0 V (corresponding to Li_2S_4 to Li_2S conversion) was also more extensive in TLE than in SLE. The ratio between the capacities corresponding to the first and second plateaus was 2.65 for TLE and 2.47 for SLE, indicating a better conversion rate of the long-chain polysulfides into Li_2S as well. As a result, the full discharge capacity of Li|TLE|S was measured as 1369 mAh/g S, a 29.4% increase from SLE electrolyte (1058 mAh/g S), and an 81.7% utilization of the theoretical capacity of elemental sulfur. The discharge capacity evolution over continuous cycling also displayed drastic differences between SLE and TLE. After 5 cycles of activation processes at 0.05 and 0.1C, two repetitions of SLE cells both showed a continuous decaying profile of discharge capacity from ∼700 mAh/g (6th cycle) to ∼300 mAh/g (50th cycle), which indicates the presence of complex electrochemical and physical processes that reduced the discharge capacity in an uncontrolled manner. For Li|TLE|S cells, despite a lower discharge capacity between 400 and 500 mAh/g after completion of activation (6th cycle, 0.2C), Li|TLE|S showed a stably increasing capacity profile with a maximum at 500−550 mAh/g S for at least 50 cycles (Figures 4B and S5). The CE for each cycle was also stable at >96%, marking a stably reversible electrochemical cycle in the Li||S cells. Comparatively, Li|SLE|S cells showed a relatively unstable CE profile and a lower average CE of ∼94% (Figure 4C).

Observation of LiPS Diffusion from S Cathode to Electrolyte in *Operando*. A combination of *ex situ* and *operando* studies was conducted to directly visualize how DSN coatings in TLE electrolyte influence polysulfide shuttling and the origins of the improved cell cycling observed above. First, we monitored the diffusion of LiPS species in SLE and TLE electrolytes. During cell cycling, confocal laser Raman microscopy can be used to spectroscopically identify and observe LiPS species (SI Section S9). We designed and improved an optical Li−S coin cell based on established implementations,[16,40] exposing a slit of polymer electrolyte at the edge of the S cathode (Figures 4D and S25B,C) through an optically flat glass window. This setup allowed real-time observation of LiPS species in the electrolyte film by confocal laser Raman mapping while operating at elevated temperature and standard coin-cell stack pressure (Figures 4E and S25A). By defining the distance of the observed LiPS signal from the edge of the S cathode as the extent of diffusion (Figures 4D and S25D), the obtained spectra series directly confirms the lateral diffusion of LiPS and allows direct comparison between shuttling in Li|SLE|S and Li|TLE|S cells (Figure 4E).

For Li|SLE|S cell, LiPS signals emerged shortly after the start of the discharge step. With further discharge to ∼12% depth of discharge (DoD, defined as currently discharged capacity/final discharged capacity × 100%), the signals of LiPS gradually diffused to an extent of >150 μm into the SLE electrolyte, with the highest intensities peaking at ∼26% DoD. This corresponds to the end of the first plateau in the capacity-voltage curve, where long-chain, high-solubility Li_2S_8, Li_2S_6, and Li_2S_4 dominate the population of LiPS species. The intensity of LiPS signals continues to increase until the DoD reaches above ∼30%, whereas the LiPS signals close to the S cathode begin to decrease. This was followed by the gradual decrease of LiPS signals from the left (edge of S cathode) to the right (furthest extent of diffusion probed) of the map, signifying the gradual diffusion of long-chain LiPS species back to the S cathode for further reduction to shorter-chain LiPS species and likely to the Li metal anode to be reduced to Li_2S. Throughout the process, the Raman signals of LiPS can be still found in all locations probed, indicating an incomplete back-diffusion of LiPS species to the cathode, corresponding to capacity loss.

Comparatively, the Li|TLE|S slit cell exhibited much lower overall LiPS signal intensities. At around 8% DoD, a low concentration of LiPS was found to evolve into the bulk TLE electrolyte, but both the signal intensity and extent of diffusion reduced quickly before ∼22% DoD, where no diffusion of LiPS into the electrolyte or residual LiPS was detected anymore. This drastic contrast supports the significant effect of TLE in reducing polysulfide species loss into the polymer electrolyte, thus mitigating the capacity loss and anode destabilization effect in Li−S cell cycling.

Retention of LiPS at S Cathode Confirmed by *Ex Situ* X-ray Absorption Spectroscopy. The mitigation of LiPS diffusion into polymer electrolyte and the retention and distribution of sulfur species in the S cathodes were further examined by *ex situ* S K-edge X-ray absorption spectroscopy on the S cathodes from disassembled Li−S full cells after discharge to different stages of discharge (Figure 4F and SI Section S10 and Figure S26). X-ray absorption near edge structure (XANES) spectra of initial S cathodes from Li|SLE|S cell were mostly composed of signals from elemental S (2472.6 eV) and LiTFSI (2479.9−2480.8 eV, outside the plotted region) after 24 h of resting in an open circuit at 80 °C. A small shoulder peak corresponding to LiPS emerged at around 2470.6 eV, likely due to LiPS produced by evaporated elemental S escaping to the Li anode. Comparatively, the S cathode from the Li|TLE|S cell showed an almost indifferentiable signal of LiPS, supporting successful blocking of LiPS diffusion and concomitant reaction with Li metal anode. After discharge to ∼2.2 V (∼16% DoD, first voltage plateau), LiPS signals (2470.8 eV, terminal $-S^-$) grew significantly in both

https://doi.org/10.1021/jacs.5c18042
J. Am. Chem. Soc. 2026, 148, 5275−5286

cells, while a more significant LiPS feature can be observed from the Li|TLE|S cell than the Li|SLE|S cell, compared against the S_8 signals at 2472.6 eV (overlapping with intrachain −S−S− signals of LiPS), showing the reduced loss of LiPS through the cathode-electrolyte interface during discharge. In further discharged S cathodes (~46% DoD, middle of the second voltage plateau), the LiPS signals were found to be more significant from the Li|TLE|S cell compared to Li|SLE|S as well, while the signal for Li_2S (2476.3 eV) grew in both cells, signifying better retention of LiPS species in the S cathode region to facilitate further reduction reactions. At the termination of discharge (100% DoD, voltage cutoff 1.5 V), LiPS signals in the Li|TLE|S cathode were significantly lower than those from the Li|SLE|S cathode when normalized against the Li_2S signal, corresponding to more complete conversion of LiPS into the final Li_2S product.

These findings are in good agreement with Li−S cell cycling results (Figure 4A,4F, left) and Raman spectroscopy (Figure 4E) showing that more LiPS was generated in the S cathode in the Li|TLE|S cell and was maintained within the S cathode during the discharge instead of spontaneous loss into the electrolyte to cause capacity loss and anode destabilization.

CONCLUSIONS

In summary, our design strategy of self-segregated trilayer polymer solid-state electrolyte improved the performance of all-solid-state Li−S batteries compared to the benchmark single-layer PEO-LiTFSI (SLE) electrolyte. Our strategy utilizes the immiscibility between PEO and an ion-selective polymer network, DSN, composed of anionic nodes and perfluorinated backbones, which phase-separates to form nanometer-thick coatings at both electrode interfaces. These coatings allow (i) the retention of LiPS species in the S cathode and suppression of shuttling into the electrolyte and eventually Li anodes, and (ii) the prevention of Li metal anode from reactive degradation with PEO, $TFSI^-$, and LiPS during static resting and dynamic cycling. These effects are enabled by selective ion conduction and chemical passivation by DSN. Through the spontaneous phase separation, these effects are localized at the critical electrode−electrolyte interfaces while preserving the bulk ion conduction properties. The resulting Li−S batteries showed improved sulfur utilization at the S cathodes, stabilization of Li metal anode, and improved cyclability in capacity retention and cycle life. We also established a method to directly spectroscopically and spatiotemporally track LiPS diffusion in the electrolyte through *operando* Raman microscopy, and the retention of LiPS species in the S cathode through *ex situ* XAS measurements. The integration of these techniques provides a characterization workflow for understanding the complex dynamics influencing the Li−S battery performance. Looking ahead, our findings provide new insights into translating knowledge from developing Li metal anode protective coatings to improving Li−S battery systems. The remaining challenges include widening the operational temperature range of the solid-state electrolyte matrix to utilize the self-segregated interfacial layer strategy to enhance the performance and extend the lifespan of Li−S batteries in broader application scenarios.

EXPERIMENTAL METHODS

Materials Preparation

Poly(ethylene oxide) (PEO, average M_v ~ 300,000), lithium bis(trifluoromethanesulfonyl)imide (LiTFSI), acetonitrile (ACN), poly(ethylene glycol) dimethyl ether (PEGDME, average M_n ~ 500), 1,2-dimethoxyethane (DME), lithium aluminum hydride ($LiAlH_4$), lithium chloride (LiCl), deuterium oxide (D_2O), and deuterated dimethyl sulfoxide (DMSO-d_6) were obtained from Sigma-Aldrich. Sulfur−carbon composite (75%), multiwall carbon nanotubes (MWCNT), and lithium discs (0.5 mm, 12 mm diameter) were obtained from MSE Supplies. Super C65 carbon was obtained from MTI Corp. Fluorinated tetraethylene glycol (FTEG) was obtained from SynQuest Laboratories. All chemicals were used without further purification. Detailed preparation of DSN, SLE, and TLE electrolytes, and S cathodes are included in SI Section S1.

Materials Characterization

Liquid-state ^{7}Li NMR spectra were recorded on a Bruker Avance 400 MHz NMR spectrometer with a Neo console at 25 °C. ^{7}Li NMR spectra was calibrated by measurement of a standard solution of 1 M $LiClO_4$ in D_2O before and after all measurements without alteration of the field. A sealed capillary insert containing DMSO-d_6 was added to each sample to maintain the locking. The sample was preserved in a dark, Ar-filled atmosphere with epoxy sealing prior to measurements. SEM micrographs were acquired on a Thermo Fisher Scientific Apreo S LoVac Scanning Electron Microscope. The samples were mounted using an air-free SEM specimen transfer holder and imaged using a beam acceleration voltage of 5 kV and a beam current of 50 pA. DSC measurements were performed using a TA Instrument Q2500 differential scanning calorimeter in a temperature range of −80 to 120 °C at a heating or cooling rate of 5 °C/min. Glass-transition temperatures (T_g) and melting temperatures (T_m) were recorded during the heating step. Nanomechanical imaging using an AFM was conducted using a Bruker Dimension Icon AFM with a Nanoscope V controller. Confocal Raman microscopy was performed on a Horiba XploRA+ confocal laser Raman microscope or a Horiba LabRAM HR Evolution Raman System with a 532 nm laser and 600 or 1200 l/mm gratings. Prior to all measurements, the Raman spectrometers were calibrated using a Si standard. Reference polymer or powder samples were sealed between two glass slides to ensure an anaerobic environment during the measurement. X-ray photoelectron spectroscopy (XPS) depth profiling of the surfaces of polymer electrolytes was performed with a PHI5000 VersaProbe III or PHI5000 VersaProbe IV XPS spectrometer. Sulfur K-edge XAS spectra were carried out at Beamline 4−3 of the Stanford Synchrotron Radiation Lightsource (SSRL) at the SLAC National Accelerator Laboratory.

Electrochemical Testing

Unless specified otherwise, all electrochemical tests were performed in standard CR2032-type coin cells. Cell fabrication details are included in SI Section S1. EIS, chronopotentiometry, chronoamperometry, and programmed procedures combining the above were performed with a BioLogic VSP, VMP3, or VSP300 potentiostat. Battery cycling procedures were performed with LAND CT3002A battery test systems or ARBIN BT2000 battery testing systems. Temperature-controlled testing and cycling were performed in an ESPEC BTU-133 environmental chamber. SS||SS cells were assembled for ionic conductivity testing, and Li||Li cells were assembled for LTN and EIS-based stability test. Li||Cu cells were assembled for Columbic efficiency determination, where the CE is defined by

$$\mathrm{CE} = \frac{C_{\mathrm{stripping}}}{C_{\mathrm{plating}}} \times 100\%$$

where C denotes the stripping and plating capacity of the respective cycling steps. Li||S cells were fabricated to test cycling performance in charge−discharge cycles and for *operando* or *ex situ* characterization experiments. In such cells, the CE is defined by

https://doi.org/10.1021/jacs.5c18042
J. Am. Chem. Soc. 2026, 148, 5275−5286

$$CE = \frac{C_{discharging}}{C_{charging}} \times 100\%$$

where C denotes the discharge and charge capacity of the respective cycling steps.

Energy Calculations

Geometry and energy calculation based on density functional theory (DFT) was performed using Jaguar *ab initio* electronic structure program[41] of the Schrödinger suite at the Sherlock computing cluster at Stanford University. Detailed fragmentation and optimization information is provided in SI Section S2.

■ ASSOCIATED CONTENT

Supporting Information

The Supporting Information is available free of charge at https://pubs.acs.org/doi/10.1021/jacs.5c18042.

Additional experimental details, characterization data, data processing and fitting details (PDF)

■ AUTHOR INFORMATION

Corresponding Authors

Yi Cui − *Department of Materials Science and Engineering and Department of Energy Science and Engineering, Stanford University, Stanford, California 94305, United States; Stanford Institute for Materials and Energy Sciences, SLAC National Accelerator Laboratory, Menlo Park, California 94025, United States;* orcid.org/0000-0002-6103-6352; Email: yicui@stanford.edu

Zhenan Bao − *Department of Chemical Engineering, Stanford University, Stanford, California 94305, United States;* orcid.org/0000-0002-0972-1715; Email: zbao@stanford.edu

Authors

Hao Lyu − *Department of Chemical Engineering, Stanford University, Stanford, California 94305, United States;* orcid.org/0000-0001-7393-2456

Xin Gao − *Department of Materials Science and Engineering, Stanford University, Stanford, California 94305, United States;* orcid.org/0000-0001-5360-0796

Lukas Michalek − *Department of Chemical Engineering, Stanford University, Stanford, California 94305, United States;* orcid.org/0000-0002-2257-5038

Tianyang Chen − *Department of Chemical Engineering, Stanford University, Stanford, California 94305, United States;* orcid.org/0000-0003-3142-8176

Weilai Yu − *Department of Chemical Engineering, Stanford University, Stanford, California 94305, United States;* orcid.org/0000-0002-9420-0702

Carina Yi Jing Lim − *Department of Materials Science and Engineering, Stanford University, Stanford, California 94305, United States*

Jacob Florian − *Department of Chemical Engineering, Stanford University, Stanford, California 94305, United States;* orcid.org/0000-0003-1895-8463

Luca Mondonico − *Department of Materials Science and Engineering, Stanford University, Stanford, California 94305, United States*

Wenbo Zhang − *Department of Materials Science and Engineering, Stanford University, Stanford, California 94305, United States*

Susmita Sarkar − *Department of Chemical Engineering, Stanford University, Stanford, California 94305, United States*

Pu Zhang − *Department of Materials Science and Engineering, Stanford University, Stanford, California 94305, United States*

Yuran Shi − *Department of Chemistry, Stanford University, Stanford, California 94305, United States;* orcid.org/0000-0003-1136-3694

Kuan-Yu Lin − *Department of Chemical Engineering, Stanford University, Stanford, California 94305, United States*

Sheng-Lun Liao − *Department of Chemical Engineering, Stanford University, Stanford, California 94305, United States*

Xueli Zheng − *Department of Materials Science and Engineering, Stanford University, Stanford, California 94305, United States; Stanford Institute for Materials and Energy Sciences, SLAC National Accelerator Laboratory, Menlo Park, California 94025, United States;* orcid.org/0000-0002-6800-2649

Jian Qin − *Department of Chemical Engineering, Stanford University, Stanford, California 94305, United States;* orcid.org/0000-0001-6271-068X

Complete contact information is available at: https://pubs.acs.org/10.1021/jacs.5c18042

Author Contributions

The manuscript was written through the contributions of all authors. All authors have given approval to the final version of the manuscript.

Notes

The authors declare the following competing financial interest(s): Z.B. and Y.C. declare that the DSN polymer used in this work is protected under the patent number US11909050B2. All other authors declare they have no competing interests.

■ ACKNOWLEDGMENTS

This work is supported by the US Department of Energy, under the Assistant Secretary for Energy Efficiency and Renewable Energy, Office of Vehicle Technologies, the Advanced Battery Materials Research (BMR) program, and the Battery500 Consortium. The authors thank Dr. Yukio Cho and Dr. Ahmed Elabd for their help with sulfur cathode preparation and characterization, Dr. Nathaniel J. Schuster for his helpful discussion on DFT calculations, Dr. Erik J. Nelson for his help with X-ray absorption measurements at the SSRL, Dr. Xuelin Guo, Mr. Antoine DeVincenti, and Dr. Byeongmoon Lee for their help with optical cell design and fabrication, Dr. Christina Newcomb for her help with the *operando* Raman microscopy measurements, and Dr. Yan-Kai Tzeng for the helpful discussion on Raman microscopy. X.Z. acknowledges the financial support provided by the US Department of Energy, Basic Energy Sciences, Materials Sciences and Engineering Division, under contract DE-AC02-76SF00515. Part of this work was performed at the Stanford Nano Shared Facilities (SNSF) RRID:SCR_023230, supported by the National Science Foundation under award ECCS-2026822. Use of the Stanford Synchrotron Radiation Lightsource, SLAC National Accelerator Laboratory, is supported by the U.S. Department of Energy, Office of Science, Office of Basic Energy Sciences under Contract No.

DE-AC02-76SF00515. Some of the computing for this project was performed on the Sherlock cluster. We would like to thank Stanford University and the Stanford Research Computing Center for providing computational resources and support that contributed to these research results.

REFERENCES

(1) Lin, D.; Liu, Y.; Cui, Y. Reviving the Lithium Metal Anode for High-Energy Batteries. *Nat. Nanotechnol.* **2017**, *12* (3), 194−206.
(2) Seh, Z. W.; Sun, Y.; Zhang, Q.; Cui, Y. Designing High-Energy Lithium−Sulfur Batteries. *Chem. Soc. Rev.* **2016**, *45* (20), 5605−5634.
(3) Zhou, G.; Chen, H.; Cui, Y. Formulating Energy Density for Designing Practical Lithium−Sulfur Batteries. *Nat. Energy* **2022**, *7* (4), 312−319.
(4) Cano, Z. P.; Banham, D.; Ye, S.; Hintennach, A.; Lu, J.; Fowler, M.; Chen, Z. Batteries and Fuel Cells for Emerging Electric Vehicle Markets. *Nat. Energy* **2018**, *3* (4), 279−289.
(5) Nazar, L. F.; Cuisinier, M.; Pang, Q. Lithium-Sulfur Batteries. *MRS Bull.* **2014**, *39* (5), 436−442.
(6) Manthiram, A.; Fu, Y.; Chung, S.-H.; Zu, C.; Su, Y.-S. Rechargeable Lithium−Sulfur Batteries. *Chem. Rev.* **2014**, *114* (23), 11751−11787.
(7) Fang, R.; Zhao, S.; Sun, Z.; Wang, D.-W.; Cheng, H.-M.; Li, F. More Reliable Lithium-Sulfur Batteries: Status, Solutions and Prospects. *Adv. Mater.* **2017**, *29* (48), No. 1606823.
(8) Yin, Y.-X.; Xin, S.; Guo, Y.-G.; Wan, L.-J. Lithium−Sulfur Batteries: Electrochemistry, Materials, and Prospects. *Angew. Chem., Int. Ed.* **2013**, *52* (50), 13186−13200.
(9) Wild, M.; O'Neill, L.; Zhang, T.; Purkayastha, R.; Minton, G.; Marinescu, M.; Offer, G. J. Lithium Sulfur Batteries, a Mechanistic Review. *Energy Environ. Sci.* **2015**, *8* (12), 3477−3494.
(10) Li, G.; Wang, S.; Zhang, Y.; Li, M.; Chen, Z.; Lu, J. Revisiting the Role of Polysulfides in Lithium−Sulfur Batteries. *Adv. Mater.* **2018**, *30* (22), No. 1705590.
(11) Wang, J.; Wang, H.; Jia, S.; Zhao, Q.; Zheng, Q.; Ma, Y.; Ma, T.; Li, X. Recent Advances in Inhibiting Shuttle Effect of Polysulfide in Lithium-Sulfur Batteries. *J. Energy Storage* **2023**, *72*, No. 108372.
(12) Bi, C.-X.; Hou, L.-P.; Li, Z.; Zhao, M.; Zhang, X.-Q.; Li, B.-Q.; Zhang, Q.; Huang, J.-Q. Protecting Lithium Metal Anodes in Lithium−Sulfur Batteries: A Review. *Energy Mater. Adv.* **2023**, *4*, No. 0010.
(13) Gao, X.; Yu, Z.; Wang, J.; Zheng, X.; Ye, Y.; Gong, H.; Xiao, X.; Yang, Y.; Chen, Y.; Bone, S. E.; Greenburg, L. C.; Zhang, P.; Su, H.; Affeld, J.; Bao, Z.; Cui, Y. Electrolytes with Moderate Lithium Polysulfide Solubility for High-Performance Long-Calendar-Life Lithium−Sulfur Batteries. *Proc. Natl. Acad. Sci. U.S.A.* **2023**, *120* (31), No. e2301260120.
(14) Kim, S. C.; Gao, X.; Liao, S.-L.; Su, H.; Chen, Y.; Zhang, W.; Greenburg, L. C.; Pan, J.-A.; Zheng, X.; Ye, Y.; Kim, M. S.; Sayavong, P.; Brest, A.; Qin, J.; Bao, Z.; Cui, Y. Solvation-Property Relationship of Lithium-Sulphur Battery Electrolytes. *Nat. Commun.* **2024**, *15* (1), No. 1268.
(15) Pan, H.; Cheng, Z.; He, P.; Zhou, H. A Review of Solid-State Lithium−Sulfur Battery: Ion Transport and Polysulfide Chemistry. *Energy Fuels* **2020**, *34* (10), 11942−11961.
(16) Gao, X.; Zheng, X.; Tsao, Y.; Zhang, P.; Xiao, X.; Ye, Y.; Li, J.; Yang, Y.; Xu, R.; Bao, Z.; Cui, Y. All-Solid-State Lithium−Sulfur Batteries Enhanced by Redox Mediators. *J. Am. Chem. Soc.* **2021**, *143* (43), 18188−18195.
(17) Su, Y.; Zhang, X.; Du, C.; Luo, Y.; Chen, J.; Yan, J.; Zhu, D.; Geng, L.; Liu, S.; Zhao, J.; Li, Y.; Rong, Z.; Huang, Q.; Zhang, L.; Tang, Y.; Huang, J. An All-Solid-State Battery Based on Sulfide and PEO Composite Electrolyte. *Small* **2022**, *18* (29), No. 2202069.
(18) Wang, D.; Jhang, L.-J.; Kou, R.; Liao, M.; Zheng, S.; Jiang, H.; Shi, P.; Li, G.-X.; Meng, K.; Wang, D. Realizing High-Capacity All-Solid-State Lithium-Sulfur Batteries Using a Low-Density Inorganic Solid-State Electrolyte. *Nat. Commun.* **2023**, *14* (1), No. 1895.
(19) Zhou, J.; Holekevi Chandrappa, M. L.; Tan, S.; Wang, S.; Wu, C.; Nguyen, H.; Wang, C.; Liu, H.; Yu, S.; Miller, Q. R. S.; Hyun, G.; Holoubek, J.; Hong, J.; Xiao, Y.; Soulen, C.; Fan, Z.; Fullerton, E. E.; Brooks, C. J.; Wang, C.; Clément, R. J.; Yao, Y.; Hu, E.; Ong, S. P.; Liu, P. Healable and Conductive Sulfur Iodide for Solid-State Li−S Batteries. *Nature* **2024**, *627* (8003), 301−305.
(20) Li, S.; Zhang, W.; Zheng, J.; Lv, M.; Song, H.; Du, L. Inhibition of Polysulfide Shuttles in Li−S Batteries: Modified Separators and Solid-State Electrolytes. *Adv. Energy Mater.* **2021**, *11* (2), No. 2000779.
(21) Zhang, Q.; Huang, Q.; Hao, S.-M.; Deng, S.; He, Q.; Lin, Z.; Yang, Y. Polymers in Lithium−Sulfur Batteries. *Adv. Sci.* **2022**, *9* (2), No. 2103798.
(22) Shan, C.; Wang, Y.; Liang, M.; Lu, K.; Xiong, C.; Hu, W.; Liu, B. A Comprehensive Review of Single Ion-Conducting Polymer Electrolytes as a Key Component of Lithium Metal Batteries: From Structural Design to Applications. *Energy Storage Mater.* **2023**, *63*, No. 102955.
(23) Stolz, L.; Hochstädt, S.; Röser, S.; Hansen, M. R.; Winter, M.; Kasnatscheew, J. Single-Ion versus Dual-Ion Conducting Electrolytes: The Relevance of Concentration Polarization in Solid-State Batteries. *ACS Appl. Mater. Interfaces* **2022**, *14* (9), 11559−11566.
(24) Judez, X.; Zhang, H.; Li, C.; Eshetu, G. G.; González-Marcos, J. A.; Armand, M.; Rodriguez-Martinez, L. M. Review—Solid Electrolytes for Safe and High Energy Density Lithium-Sulfur Batteries: Promises and Challenges. *J. Electrochem. Soc.* **2018**, *165* (1), No. A6008.
(25) Fenton, D. E.; Parker, J. M.; Wright, P. V. Complexes of Alkali Metal Ions with Poly(Ethylene Oxide). *Polymer* **1973**, *14* (11), No. 589.
(26) Berthier, C.; Gorecki, W.; Minier, M.; Armand, M. B.; Chabagno, J. M.; Rigaud, P. Microscopic Investigation of Ionic Conductivity in Alkali Metal Salts-Poly(Ethylene Oxide) Adducts. *Solid State Ionics* **1983**, *11* (1), 91−95.
(27) Pożyczka, K.; Marzantowicz, M.; Dygas, J. R.; Krok, F. Ionic Conductivity and Lithium Transference Number of Poly(Ethylene Oxide):LiTFSI System. *Electrochim. Acta* **2017**, *227*, 127−135.
(28) Yu, Z.; Mackanic, D. G.; Michaels, W.; Lee, M.; Pei, A.; Feng, D.; Zhang, Q.; Tsao, Y.; Amanchukwu, C. V.; Yan, X.; Wang, H.; Chen, S.; Liu, K.; Kang, J.; Qin, J.; Cui, Y.; Bao, Z. A Dynamic, Electrolyte-Blocking, and Single-Ion-Conductive Network for Stable Lithium-Metal Anodes. *Joule* **2019**, *3* (11), 2761−2776.
(29) Perdew, J. P.; Wang, Y. Accurate and Simple Analytic Representation of the Electron-Gas Correlation Energy. *Phys. Rev. B* **1992**, *45* (23), No. 13244.
(30) Han, Y.-K.; Jung, J.; Yu, S.; Lee, H. Understanding the Characteristics of High-Voltage Additives in Li-Ion Batteries: Solvent Effects. *J. Power Sources* **2009**, *187* (2), 581−585.
(31) Cumpson, P. J.; Portoles, J. F.; Barlow, A. J.; Sano, N. Accurate Argon Cluster-Ion Sputter Yields: Measured Yields and Effect of the Sputter Threshold in Practical Depth-Profiling by x-Ray Photoelectron Spectroscopy and Secondary Ion Mass Spectrometry. *J. Appl. Phys.* **2013**, *114* (12), No. 124313.
(32) Yusim, Y.; Moryson, Y.; Seipp, K.; Sann, J.; Henss, A. Challenges in XPS Analysis of PEO-LiTFSI-Based Solid Electrolytes: How to Overcome X-Ray-Induced Photodecomposition. *Batteries Supercaps* **2024**, *7* (10), No. e202400161.
(33) Derjaguin, B. V.; Muller, V. M.; Toporov, Y. P. Effect of Contact Deformations on the Adhesion of Particles. *J. Colloid Interface Sci.* **1975**, *53* (2), 314−326.
(34) Takeoka, S.; Ohno, H.; Tsuchida, E. Recent Advancement of Ion-Conductive Polymers. *Polym. Adv. Technol.* **1993**, *4* (2−3), 53−73.
(35) Stolz, L.; Homann, G.; Winter, M.; Kasnatscheew, J. The Sand Equation and Its Enormous Practical Relevance for Solid-State Lithium Metal Batteries. *Mater. Today* **2021**, *44*, 9−14.
(36) Stolz, L.; Hochstädt, S.; Röser, S.; Hansen, M. R.; Winter, M.; Kasnatscheew, J. Single-Ion versus Dual-Ion Conducting Electrolytes:

https://doi.org/10.1021/jacs.5c18042
J. Am. Chem. Soc. 2026, 148, 5275−5286

the Relevance of Concentration Polarization in Solid-State Batteries. *ACS Appl. Mater. Interfaces* **2022**, *14* (9), 11559−11566.
(37) Luo, Y.; Gao, L.; Kang, W. A New Review of Single-Ion Conducting Polymer Electrolytes in the Light of Ion Transport Mechanisms. *J. Energy Chem.* **2024**, *89*, 543−556.
(38) Evans, J.; Vincent, C. A.; Bruce, P. G. Electrochemical Measurement of Transference Numbers in Polymer Electrolytes. *Polymer* **1987**, *28* (13), 2324−2328.
(39) Song, Y.-W.; Shen, L.; Li, X.-Y.; Zhao, C.-X.; Zhou, J.; Li, B.-Q.; Huang, J.-Q.; Zhang, Q. Phase Equilibrium Thermodynamics of Lithium−Sulfur Batteries. *Nat. Chem. Eng.* **2024**, *1*, 588−596.
(40) Zhang, W.; Sayavong, P.; Xiao, X.; Oyakhire, S. T.; Shuchi, S. B.; Vilá, R. A.; Boyle, D. T.; Kim, S. C.; Kim, M. S.; Holmes, S. E.; Ye, Y.; Li, D.; Bent, S. F.; Cui, Y. Recovery of Isolated Lithium through Discharged State Calendar Ageing. *Nature* **2024**, *626* (7998), 306−312.
(41) Bochevarov, A. D.; Harder, E.; Hughes, T. F.; Greenwood, J. R.; Braden, D. A.; Philipp, D. M.; Rinaldo, D.; Halls, M. D.; Zhang, J.; Friesner, R. A. Jaguar: A High-Performance Quantum Chemistry Software Program with Strengths in Life and Materials Sciences. *Int. J. Quantum Chem.* **2013**, *113* (18), 2110−2142.

https://doi.org/10.1021/jacs.5c18042
J. Am. Chem. Soc. 2026, 148, 5275−5286